UC Berkeley
UC Berkeley Previously Published Works

Title

Impacts of Dissolved Iron on Alkaline Water Electrolysis Cells

Permalink

Journal

ISSN

Authors

Rajeev, Manasa

Jerome-Saboori, Arya

Shekhar, Raj

et al.

Publication Date

DOI

Copyright Information

Peer reviewed

Impacts of dissolved iron on alkaline water electrolysis cells

Manasa Rajeev,[1,2] Arya Jerome-Saboori,[1,2] Raj Shekhar,[1,2] Shannon W. Boettcher,[1,2,3*] Paul A. Kempler[1,2*]

[1] *Department of Chemistry and Biochemistry, University of Oregon, Eugene, OR 97403*

[2] *Oregon Center for Electrochemistry, University of Oregon, Eugene, OR 97403*

[3] *Department of Chemical & Biomolecular Engineering and Department of Chemistry, University of California, Berkeley, and Energy Storage and Distributed Resources Division, Lawrence Berkeley National Laboratory, Berkeley, CA 94720, United States.*

[*]Correspondence: boettcher@berkeley.edu
[*]Correspondence: pkempler@uoregon.edu

Abstract:

Dissolved iron (Fe) species are a pre-requisite for the most active catalyst sites for the oxygen evolution reaction in alkaline electrolytes, but the overall effects of dissolved Fe on energy-efficient advanced alkaline water electrolysis cells remain unclear. Here, we systematically control the concentration of Fe in a model zero-gap alkaline water electrolyzer to understand the interactions between Fe and high surface area catalyst coatings. Cells employing a platinum-group-metal-containing cathode and a high surface area, mixed-metal-oxide anode yielded an optimum voltage efficiency at elevated temperatures and in the presence of 6 ppm Fe, which reduced the cell voltage by ~100 mV compared to rigorously Fe-free electrolytes. Increasing concentrations of Fe led to a systematic increase in anode activity towards the oxygen evolution reaction and a reduction in the electrochemically active surface area at both the anode and cathode. Metallic Fe was not observed to electrodeposit at cathodes which operate at overpotentials ≤ 120 mV, but dissolved Fe does reduce the apparent number density of sites available for hydride adsorption. These findings suggest that the energy efficiency of advanced alkaline water electrolysis systems can be improved by managing the Fe concentration in recirculating KOH electrolytes.

Introduction

Alkaline water electrolysis (AWE) is the most-mature and scalable approach to electrolytic hydrogen production.[1–3] Electrodes used for alkaline water-splitting reactions can be manufactured from earth-abundant transition metals (e.g., Ni, Fe, Co, and Mn)[4–6] and most often operate at temperatures ~80 °C in highly alkaline conditions (5–7 M KOH) to maximize the ionic conductivity of the electrolyte and minimize activation overpotentials at the anode and cathode.[3,7] Electrocatalysts used in industrial AWE designs have historically been composed of high-surface-area metals (e.g. Raney Ni)[8] or metal oxides that can be coated onto metal meshes at the m^2 scale. These electrodes last for years of continuous operation because they form active oxyhydroxide catalytic layers at their operating potentials that kinetically stabilize the underlying oxide and metal support in the alkaline environment. Although traditional AWE designs operate at current densities ($0.2–0.4$ A cm^{-2}) that are below those of membrane electrolysis (~2 A cm^{-2}),[9] modern advanced alkaline water electrolysis (AAWE) designs minimize the ohmic resistance at the electrode-diaphragm junction and can support current densities > 1 A cm^{-2} at 1.6 V over small-cell areas.[10–12]

The electrocatalytic activity of materials used for AWE may be substantially improved through electrolyte design. The concentration and identity of supporting cations influence the reaction environment at electrocatalyst surfaces and thus affect the rate of the hydrogen evolution reaction (HER) and oxygen evolution reaction (OER).[13–17] The rate of the HER at Au(111) and polycrystalline (pc) Au surfaces is highest when weakly solvated alkali-metal hydroxides (e.g. CsOH) serve as the supporting electrolyte, whereas the opposite trend is observed for Pt(111) and pc-Pt.[16,18] The overpotential towards the OER at Ni(Fe)OOH increases by ~100 mV in 0.10 M LiOH electrolytes as compared to 0.10 M CsOH, whereas the addition of 1 mM Ca(OH)$_2$ to 0.10 M KOH leads to a similar 60 mV increase in anode overpotential.[19,20]

Electrodes for the OER are particularly sensitive to Fe at ppm (µM) concentrations: intentional doping of NiO_x anodes with 0.1% Fe resulted in a decrease in the OER overpotential in over 130 mV,[21] and adventitious incorporation of < 36 ppb Fe in 1 M KOH decreased the OER overpotential of thin-film β-NiOOH by 100 mV as compared to a purified KOH electrolyte.[22] Corrigan reported that the addition of ~10% of Fe into thin film NiO electrodes in 25% w/w KOH at 25 °C led to a decreased Tafel slope by 25 mV dec^{-1} suggesting a synergic effect of Fe and Ni towards catalyzing the OER reaction.[21] Recently Ou et al. found that electrodes with surface Fe yield the greatest activity on a per-Fe-basis and that the Tafel slope shifts from ~60 to ~30 mV dec^{-1} for NiOOH cycled in an electrolyte containing >0.1 ppm [Fe] as Fe accumulates at the electrocatalyst surface.[23] Demnitz reported that dissolved Fe species lowered the OER overpotential at uncoated Ni meshes in 30% w/w unpurified KOH at temperatures 75–90 °C at current densities up to 800 mA cm^{-2}.[24]

The effects of Fe on cathodes used for alkaline water electrolysis are varied. Markovic reported the activation of Pt(111) surfaces towards the HER in 0.10 M KOH via modification with $Ni(OH)_2$ and later Xue et al. showed that Ni-Fe-modified Pt(111) surfaces show enhanced performance for alkaline HER relative to Ni-modified Pt.[25] Likewise, Fe has a beneficial effect on the HER activity of uncoated Ni electrodes in 30% w/w KOH.[24] However, Fe has been reported to deactivate Ni meshes coated with platinum-group metals (PGMs) when operated in chlor-alkali environments (33% w/w NaOH at 90 °C), leading to a 100 mV cathodic shift for the HER overpotential when Fe was present at 1 ppm as compared to commercial NaOH.[26]

The impacts of dissolved Fe are important to understand and control in AWE systems as Fe is present in ppm quantities in commercial KOH, and additional Fe can be spontaneously leached from stainless-steel cell components contacting recirculated electrolytes. Although the beneficial effect of dissolved Fe in concentrated KOH on both OER and HER kinetics for uncoated

Ni electrodes has been well explored in low-temperature analytical experiments,[24] the interactions between Fe and catalyst layers used in energy-efficient cells has not been characterized in conditions consistent with industrial electrolyzers. Model AAWE cells are necessary to evaluate these impacts, as the effects of dissolved Fe on high-surface-area electrocatalyst coatings operated at high current densities are likely controlled by the local environment (ionic strength, pH, temperature, dissolved Fe concentration, electrochemical potential) produced at anode and cathode active sites.

Here, we quantify the effects of dissolved Fe at a model AAWE cell with various transition-metal-oxide anode catalysts and a PGM coated cathode.[27] We find that dissolved Fe impacts electrocatalysts used in AAWE cells in a manner that is distinct from cells composed of pure Ni electrodes or electrocatalysts operated in [KOH] $\leq$ 1 M, with an optimum dissolved [Fe] concentration existing within the range of [Fe] attainable for recirculated KOH electrolytes. These findings have important implications for the design of systems for hydrogen production with recirculated KOH and the design of alkaline electrocatalyst coatings.

Materials and methods

Materials: Nickel (II) nitrate hexahydrate, $Ni(NO_3)_2 \cdot 6H_2O$ (99.99%), cobalt (II) nitrate hexahydrate, $Co(NO_3)_2 \cdot 6H_2O$ (99.99%), iron (II) chloride tetrahydrate, and $FeCl_2 \cdot 4H_2O$ (> 99%,), were purchased from Sigma Aldrich. Potassium hydroxide, KOH (99.99% trace metals basis) was purchased from Thermo Fischer. ICP-MS-grade HNO_3 (Sigma Aldrich) was used to prepare stock solutions of dissolved Fe for ICP-MS analysis. Ni mesh (99.7% metals basis) was purchased from Fuel Cell Materials and impurities were identified using X-ray photoelectron spectroscopy (XPS) (**Table S1, Figure S1**). All solutions were prepared from deionized water (H_2O) having a resistivity >18.2 MΩ-cm was obtained from a Millipore Milli-Q water purification

system. Stock solutions of 1 mM $FeCl_2 \cdot 4H_2O$ were prepared in 10 mM HNO_3 to ensure complete dissolution.

Electrode preparation: Ni meshes (2 cm x 2 cm) were acid-cleaned in a 20% v/v $HCl_{(aq)}$ solution for 2 min, before coating. $Ni(Co)O_xH_y$ (NiCo) anodes were deposited from a solution containing 0.50 M $Ni(NO_3)_2$ and 0.50 M $Co(NO_3)_2$ in H_2O at 20 °C via five sequential cathodic depositions at -100 mA cm^{-2} for 1 min each followed by thermal annealing at 400 °C for 15 min each cycle in air. NiO_xH_y coated Ni mesh electrodes (NiO) were prepared via five sequential cathodic electrodepositions with a constant current of -100 mA cm^{-2} for 30 s each from a precursor solution of 0.5 M $Ni(NO_3)_2$ at 20 °C followed by thermal annealing at 400 °C for 15 min each cycle in air. Uncoated Ni mesh (Ni) electrodes were acid-cleaned in 20% v/v $HCl_{(aq)}$ immediately before assembly and testing. A PGM coated cathode was obtained from De Nora Tech LLC.

Two-electrode measurements: All electrochemical measurements were collected using a BioLogic SP-300 instrument. A model AAWE cell was machined out of polyether ether ketone (PEEK), where the anode and cathode meshes (1 cm^2 projected area) were compressed on either side of the separator (Zirfon-220, 1.5 cm^2) to enforce a zero-gap geometry (**Figure 1a, Figure S2**). Prior to all experiments, electrodes were pre-conditioned in 30% w/w KOH at 80 °C for 1 h at a current density *J,* of 250 mA cm^{-2}. The total cell volume contained 20 mL of electrolyte, and the solution was continuously stirred at 240 rpm using a small magnetic stir bar to help remove the produced gases from the electrolyte (**Figure 1a**). During extended testing, a syringe pump was connected to the AAWE cell to replace evaporated H_2O at a flow rate of 2.7 μL min^{-1} which maintained a stable concentration of KOH.

Three-electrode measurements: Cyclic voltammetry studies were performed on electrodes in the zero-gap assembly with Ni mesh serving as the counter electrode and a reversible hydrogen electrode (RHE, Gaskatel Hydroflex) serving as the reference (**Figure 1a**). For studies on cathode

activity, the electrode potential was measured at -250 mA cm^{-2}, with occasional polarizations at 0.500 V vs. RHE used to understand the behavior of adsorbed species during electrolyzer shutdown and galvanostatic electrochemical impedance spectroscopy (GEIS) measurements used to monitor the changes in the ohmic resistance of the cell.

Material Characterization: Surface morphology analysis was performed by scanning electron microscopy (SEM, Thermo Fischer Apreo 2) using an accelerating voltage of 5–15 keV and an in-lens detector. X-ray Photoelectron Spectroscopy measurements were conducted using a Thermo-Scientific ESCALAB 250 instrument with a non-monochromatic Mg-Kα source (200W, 40 eV pass energy). A low-energy electron flood source was used for charge neutralization. Powder X-ray diffraction (PXRD) data were obtained using a Bruker D2 phaser equipped with a Cu Kα source (wavelength = 1.54 Å) over a 2θ range of 20–70° with a step size of 0.2°.

In-situ Raman measurements: Electrodes were tested in a custom *in-situ* Raman cell (Figure SI) with Ni wire serving as the counter electrode and Hg/HgO as the reference electrode. The Raman objective lens was covered with a thin, translucent film of (poly)tetrafluoroethylene and immersed in the electrolyte to improve collection from the working electrode surface. The electrode was preconditioned at $J = 250$ mA cm^{-2} prior to the measurement. Cyclic voltammetry was collected before and after adding dissolved Fe (as FeCl$_2$ · 4H$_2$O). Raman spectra were collected under constant potential after a 2 min stabilization period using a 5 mW red laser (633 nm) and each spectra represents the average of 5 acquisitions (**Figure S3**).

Results

PGM-coated Ni meshes served as high-activity cathodes (**Figure 1e**) and were assembled with transition-metal-oxide-coated Ni mesh anodes (**Figure 1b**) into diaphragm-electrode packages and compressed to a final thickness of 562 μm (**Figure 1a**). A thick Ni(Co)O$_x$H$_y$ coating

was prepared to simulate coatings prepared on commercial AWE anodes.[28,29] SEM images of the annealed $Ni(Co)O_xH_y$ coating showed a layered surface texture, which yielded a powder XRD pattern consistent with a $Ni_zCo_{(1-z)}O_x$ spinel phase (**Figures S4-S5**).[28] Anode cross sections were prepared using an Ar-plasma focused-ion beam and imaged via SEM to characterize the coating thickness and interface morphology. The PGM coating was a porous layer that was μm-scale in total thickness (**Figure 1e**). The $Ni(Co)O_xH_y$ catalyst coating was uniform with a total film thickness of ~1 μm but had wide cracks with separated domains and nanoscale pores distributed across the coating surface (**Figure 1d**).

To study the influence of the dissolved concentration of Fe, [Fe], on the electrochemical behavior of the cell, 1.0 mM $FeCl_2$ was incrementally added to 30% w/w KOH electrolyte preheated to 20 or 80 °C to a final [Fe] = 3.0–24 ppm. Fe^{2+} was selected as the source of dissolved Fe because of the greater solubility of ferrous species, although Fe oxidizes to Fe^{3+} in the presence of dissolved O_2. Separate additions of Cl^- (as KCl) showed no substantial impact on the activity of either NiCo or PGM electrodes (**Figure S6, Table S2**). Further increases to [Fe] were not investigated because the formation of precipitates was observed for [Fe] > 24 ppm.

We first compared the effect of [Fe] on the cell voltage for a series of electrodes and operating temperatures. The impact of increasing [Fe] on the total cell voltage, E_{cell}, was recorded at $J = 250$ mA cm^{-2} and was sensitive to both the operating temperature as well as the cathode composition (**Figure 2a**). A platinum-group-metal-free cell prepared using a Ni cathode and a NiCo anode (Ni-NiCo) produced $2.15 < E_{cell} < 2.45$ V at 20 °C with the lowest E_{cell} observed for [Fe] = 17 ppm, whereas the use of a commercial cathode (PGM-NiCo) yielded $1.85 < E_{cell} < 2.05$ V at 20 °C, with an optimal [Fe] of 12 ppm. Data was not collected for [Fe] > 24 ppm for cells at 20 °C due to spontaneous precipitation of solid Fe species. The same PGM-NiCo cell operated at 80 °C produced $E_{cell} < 1.8$ V for all [Fe] < 35 ppm, with the lowest $E_{cell} = 1.77(7)$ V observed at [Fe] = 6 ppm. Thus, rigorous control of the dissolved concentration of Fe afforded an improvement to E_{cell} at all operating temperatures. A 200–250 mV improvement in E_{cell} was observed at 20 °C as compared to a 100 mV improvement to E_{cell} at 80 °C, with the lower [Fe] required for peak cell performance as compared to an unheated cell. E_{cell} for the PGM-NiCo cell decreased by ~90 mV
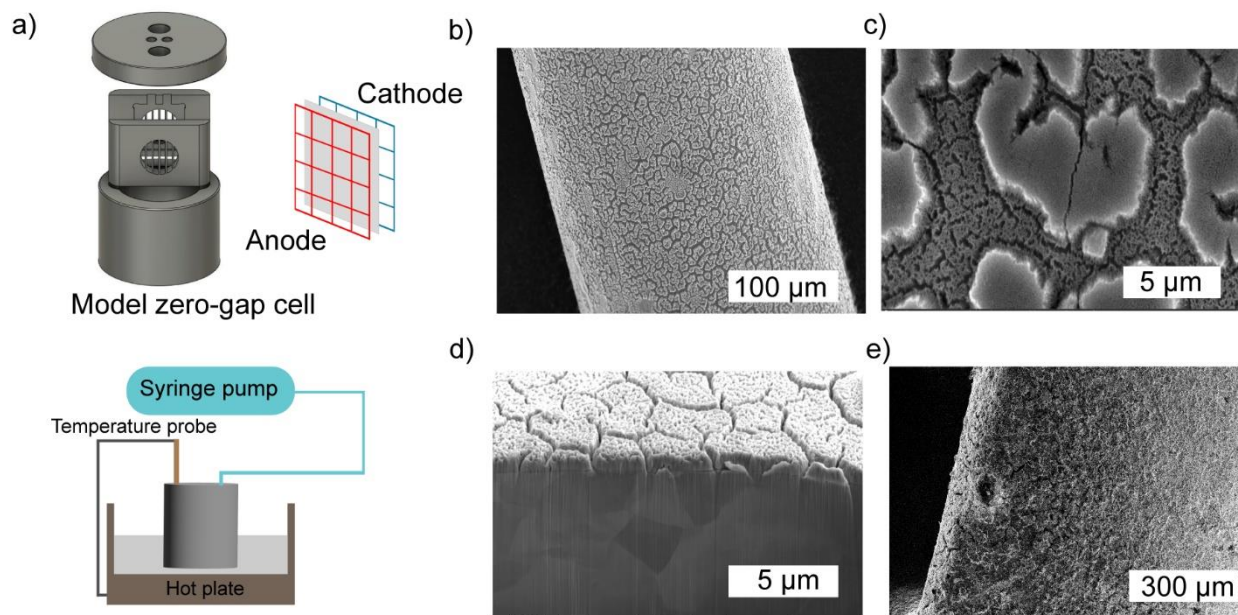

Figure 1: (a) Schematic diagram of the model zero-gap AAWE cell showing the diaphragm-electrode assembly. **(b, c)** SEM image of the Ni(Co)O$_x$H$_y$ anode prepared in this work. **(d)** Focused ion beam (FIB) cross-section of Ni(Co)O$_x$H$_y$ coating on Ni mesh. **(e)** SEM image of a commercial high-surface-area cathode.

at a current density of $J = 250$ mA cm^{-2} after adding 6 ppm of Fe compared to KOH with [Fe] = 0 ppm. The concentration of Fe stabilized approximately 4.5 ppm within 30 min, after which E_{cell} was stable. (**Figure S7-S8**).

Polarization curves were recorded for the top-performing AAWE configuration to investigate the mechanistic effects of [Fe] on electrolyzer behavior. **Figure 2b** shows the change in E_{cell} for PGM-NiCo cells during a series of galvanostatic holds from $J = 10–400$ mA cm^{-2} at varied [Fe] (0–24 ppm). Each E_{cell} value was recorded after 5 min of applied current. At [Fe] = 6 ppm, $E_{cell} = 1.90(7)$ V was obtained at $J = 400$ mA cm^{-2}, which was > 80 mV less than the next-most-optimal E_{cell} values recorded for [Fe] = 3 and 12 ppm. E_{cell} decreased with increasing [Fe] from 0 to 6 ppm but then increased for further increases to [Fe]. The maximum impact of modifying [Fe] within a practical range for an industrial AWE cell was a 350 mV difference in E_{cell} at $J = 400$ mA cm^{-2}.
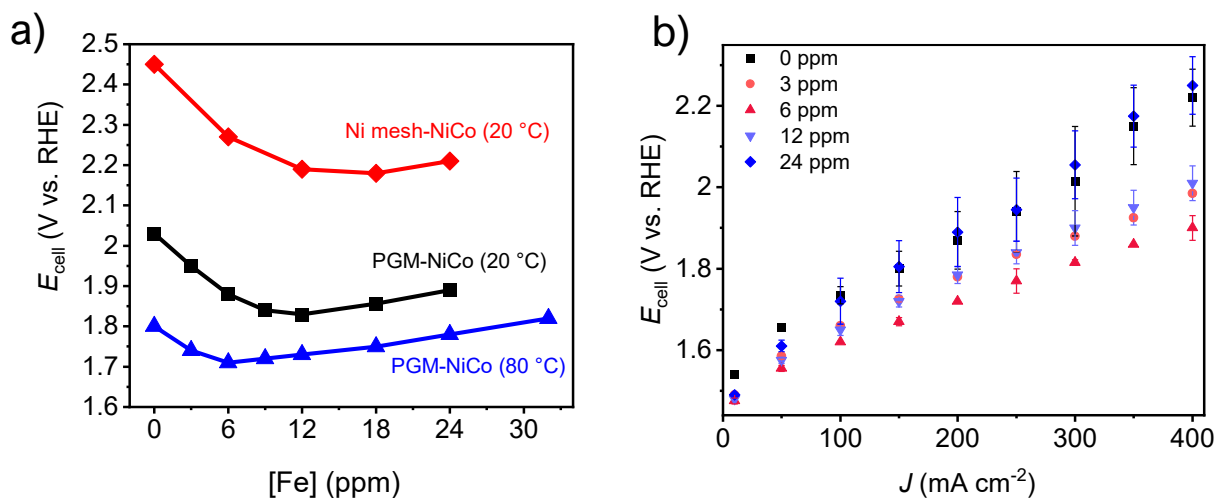

Figure 2: (a) Effect of Fe on the total cell voltage at $J = 250$ mA cm^{-2} as a function of the cell assembly and operating temperature. **(b)** J-E_{cell} behavior of PGM-NiCo AAWE cells at 80 °C for various Fe concentrations. Error bars represent one standard deviation across three independent AAWE cell trials.

The long-term effect of dissolved Fe on AAWE cell voltage was studied by recording periodic galvanostatic electrochemical impedance spectra at a PGM-NiCo cell at 80 °C and $J = 250$ mA cm^{-2} for 150 h (**Figure 3**). E_{cell} remained < 1.71 V for 150 h with an average increase of 27 µV h^{-1} and R_Ω was stable at 0.33 ± 0.01. The positive impact of trace Fe on the overall cell performance was persistent and no evidence of deleterious impacts on the resistance of the separator was observed.

To understand the sensitivity of our results to the composition and design of the anode catalyst coating, we collected a series of cyclic voltammograms for three different anodes in 30% w/w KOH at 80 °C as a function of [Fe] (**Figure 4**). For the NiCo anode in [Fe] = 0 ppm electrolyte, a broad oxidation wave at $E_{\text{anode}} = 1.25$ V was assigned to Co$^{2+/3+}$ redox,[30] with an overlapping wave at $E_{\text{anode}} = 1.34$ V assigned to Ni$^{2+/3+}$ redox.[22] A single oxidation

Figure 3: E_{cell} vs time behavior for PGM-NiCo AAWE cell at $J = 250$ mA cm^{-2} with [Fe] = 6 ppm. The ohmic resistance (R_Ω) was measured via GEIS at 200 kHz–100 mHz at $J = 250$ mA cm^{-2} every 20 h.

wave at 1.40 V was observed for the Ni and NiO electrodes, assigned to Ni$^{2+/3+}$ states, with an additional irreversible wave at 1.48 V assigned to the oxidation of Ni^{3+} prior to the onset of oxygen evolution. Increasing [Fe] led to a positive shift in the oxidation and reduction waves for the NiCo anode and a substantial reduction in the integrated charge under both peaks, Q_{anode}, which was quantified (**Table 1**) from the cathodic wave to avoid the onset of the oxygen evolution reaction:

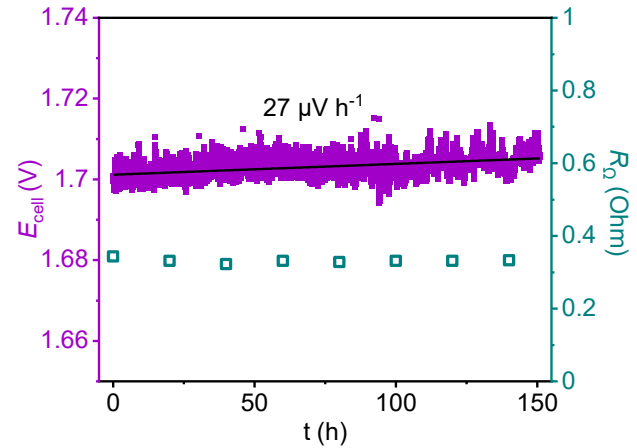$$Q_{\text{anode}} = \frac{1}{\nu} \int_{1.25}^{1.1} J \, dE \qquad (1)$$

Q_{anode} for NiCo anodes systematically decreased for increasing [Fe] from 22.3 mC cm^{-2} in Fe-free electrolyte to 3.2 mC cm^{-2} in the presence of 24 ppm Fe.

Similar shifts in peak potential occurred for both the Ni and NiO anodes. With the addition of Fe to 6 ppm, the Ni$^{3+/4+}$ oxidation wave seen at NiO was no longer separable from the catalytic current towards the OER. For all anodes, a single reduction peak was observed, corresponding to the Ni^{3+}/Ni^{2+} and Co^{3+}/Co^{2+} transitions. At [Fe] = 0 and 6 ppm for NiCo and Ni electrodes, the cathodic peak potential (E_p^c) was observed at 1.2 V and 1.19 V, respectively, which shifted positively to 1.24 V at [Fe] = 24 ppm. For the NiO electrode, the E_p^c shifted from 1.2 V to 1.25 V as the [Fe] increased from 0 to 24 ppm. Comparing a high [Fe] electrolyte to an Fe-free electrolyte, Q_{anode} at the NiO anode decreased from 36.4 mC cm^{-2} to 24.8 mC cm^{-2}, but increased from 9.9 mC cm^{-2} to 19.1 mC cm^{-2} for the bare Ni electrode indicating that Fe has differing impacts on the quantity of apparent redox-active metal oxide-hydroxide sites which are related to the electrochemically active surface area depending on the initial surface structure and composition of the anode.[31]
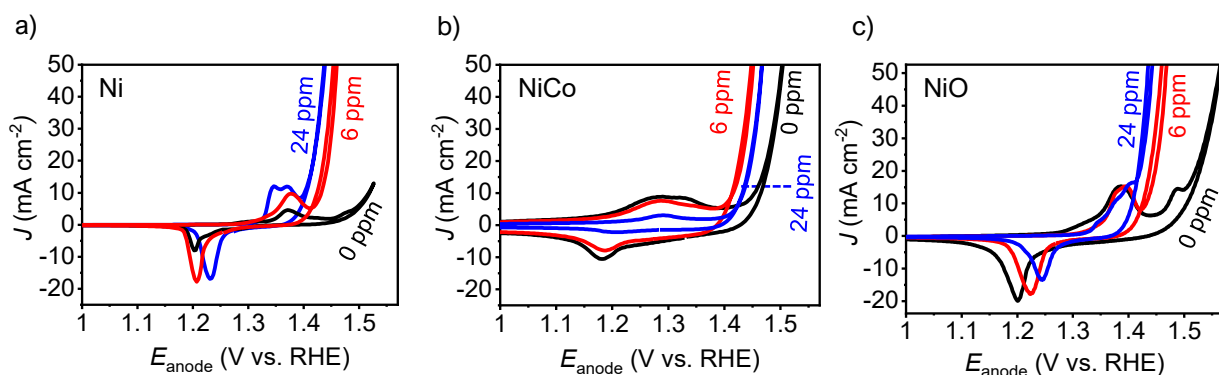

Figure 4: Cyclic voltammograms collected with **(a)** Ni anode, **(b)** NiCo anode **(c)** NiO anode after 60 min of conditioning in 30% w/w KOH at 80 °C at 250 mA cm^{-2} and then cycled in three different [Fe] at a scan rate (v) = 20 mV s^{-1}. Data is shown for the second voltammetry cycle.

The effect of increasing [Fe] had qualitatively distinct effects on the NiCo anode as compared to the Ni and NiO anodes. Electrode activity was benchmarked as η_{50}, the overpotential required to reach $J = 50$ mA cm^{-2} towards the OER. The NiCo anode was the most-active OER electrode in [Fe] = 0 ppm electrolyte, exhibiting η_{50} that was 50 mV less positive than NiO, consistent with the higher intrinsic activity of Co-based oxides over Fe-free Ni-based systems.[30,32] The activity of all three electrodes increased dramatically with a small increase in [Fe] to 6 ppm. The NiCo anode had the lowest $\eta_{50} = 261$ mV whereas the uncoated Ni was slightly more active than the NiO anode ($\eta_{50} = 273$ and 280 mV, respectively). This can be understood from the low tafel slopes for NiCo anode compared to both NiO and Ni mesh anodes. (**Figures S9-S11**) Additional dissolved Fe led to an increase in η_{50} to 280 mV for the NiCo anode whereas the uncoated Ni and NiO anodes continued to improve with increasing [Fe], yielding $\eta_{50} = 246$ and 260 mV, respectively.
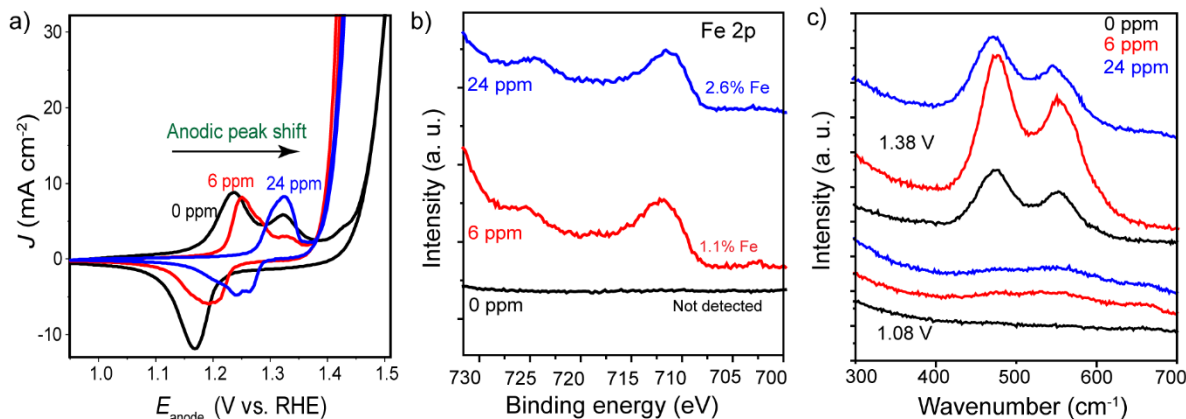
Figure 5: (a) Cyclic voltammogram of NiCo anode at 0, 6, and 24 ppm Fe concentration in 30% w/w KOH at 80 °C at $v = 20$ mV s^{-1} after 24 h of continuous polarization at 250 mA cm^{-2} **(b)** Background-corrected XPS spectra in the Fe2p region for the NiCo anodes. The elemental composition has been calculated by the ratios of the integrated peak areas **(c)** *In-situ* Raman spectra of NiCo electrode in 30 wt% KOH at 60 °C recorded at 1.08 V and 1.38 V vs RHE.

We conducted extended constant current testing at $J = 250$ mA cm^{-2} for various [Fe] on three otherwise untested NiCo anodes and quantified the surface-Fe content using X-ray photoelectron spectroscopy (XPS, **Figure 5b, Figure S12**). The amount of Fe measured on the anode surface increased monotonically with the initial concentration of Fe within the cell. The elemental composition was estimated on a metals basis, normalizing the integrated Fe $2p_{3/2}$ region to the total Ni and Co content within the anode surface. NiCo electrodes exhibited an increasingly Fe-rich surface with increasing [Fe], with a reduction in the apparent Ni content after testing in 24 ppm Fe (**Table S1**). Cyclic voltammetry of the NiCo anodes after 24 hours of continuous operation showed a qualitative change in peak shape and a reduction in Q_{anode} relative to the as-deposited electrodes (**Figure 5a**). The decrease in Q_{anode} was similar for [Fe] = 6 and 24 ppm but only a single anodic wave with a peak at $E_{anode} = 1.35$ V was observed for [Fe] = 24 ppm. To further understand the effect of dissolved Fe on the compositional and structural changes at the NiCo anode, *in-situ* Raman measurements were conducted at 60 °C at constant E_{anode} (**Figure 5 c, Figure S13**). The two prominent Raman peaks observed at 474-477 cm^{-1} (P1) and 549-555 cm^{-1} (P2) have previously been assigned to Ni-O bending mode (E_g) and stretching mode (A_{1g}) vibrations, respectively.[33,34] For $E_{anode} = 1.08$–1.38 V, the peak intensity first increased with the addition of Fe to the electrolyte at 6 ppm and subsequently decreased for [Fe] = 24 ppm. At $E_{anode} = 1.08$ V, no peaks were found in the region 400 to 600 cm^{-1} for [Fe] = 0 ppm, while two peaks were observed at 479 cm^{-1} and 551 cm^{-1} when the Fe concentration was increased to higher concentrations. At all [Fe] for $E \geq 1.23$ V we did not observe any additional peaks besides those assigned to Ni-O vibrations in oxyhydroxide materials. The stability of PGM cathodes was evaluated while driving the HER at $J = -250$ mA cm^{-2} with an uncoated Ni mesh serving as a counter electrode to avoid the influence of dissolution products from anode coatings. Increasing [Fe] led to increasing absolute cathode overpotentials, $\eta_{cathode}$, for all [Fe], with $\eta_{cathode}$ reaching a steady state value

within 30 min (**Figure 6a**). The average rate of cathode deactivation during the first 20 min at 0, 3, 6, and 24 ppm of Fe were 1.6, 5.1, 6.3, and 8.1 mV h^{-1}, respectively.

Previously, Fe has been observed to accumulate at AWE cathodes, so we tested the response of $\eta_{cathode}$ to a short-term anodic bias at $E_{cathode} = 0.500$ V vs RHE, which was sufficiently positive to oxidize and strip dissolved Fe^{2+} species.[35] At [Fe] = 6 ppm, $\eta_{cathode}$ shifted positive by < 10 mV for a short time following anodic bias but the effect was not preserved; no shift in $\eta_{cathode}$ was observed following anodic bias for the cathode tested in [Fe] = 24 ppm (**Figure 6b**). The influence of [Fe] on $\eta_{cathode}$ for PGM cathodes was also assessed over 50 h of continuous testing at $J = -250$ RmA cm^{-2} in an 80 °C electrolyte with [Fe] = 24 ppm (**Figure 6c**). After the initial negative shift in $\eta_{cathode}$ over 30 mins following the addition of Fe, $\eta_{cathode}$ moved slowly positive to a steady-state value of ~ –100 mV. A 20 min potentiostatic hold at 0.500 V led to a < 10 mV positive shift which was reversed after ~30 min of continued cathodic bias at $J = -250$ mA cm^{-2}.
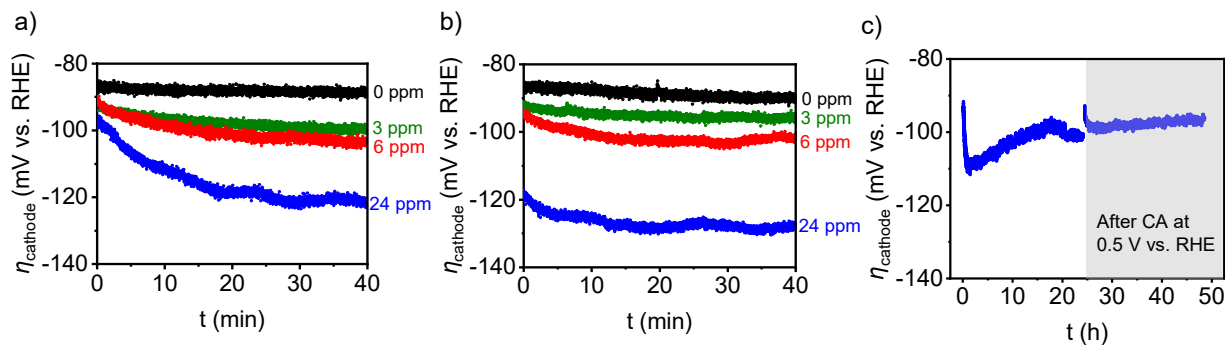

Figure 6: **(a)** Galvanostatic measurement of the PGM cathode as working electrode at –250 mA cm^{-2} with a Ni mesh counter electrode and RHE reference at different [Fe]; **(b)** after reverse polarization at 0.500 V vs. RHE for 20 min. **(c)** Cathodic galvanostatic measurement of the PGM cathode as the working electrode at –250 mA cm^{-2} with a Ni mesh counter electrode, and RHE reference electrode in 24 ppm Fe. The electrode was polarized at 0.500 V vs. RHE for 20 minutes at $t = 24$ h.

Voltammetry of PGM cathodes showed that the HER onset potential was sensitive to [Fe] (**Figure 7b**). Hysteresis was observed in the HER region, with a more positive $\eta_{cathode}$ at $J = 50$ mA

cm^{-2} observed during the positive-direction sweep for voltammetry in [Fe] = 0 ppm and 6 ppm.

Voltammetry in 30% w/w KOH at 80 °C prior to the production of dissolved H_2 and O_2 was performed to measure the response of the hydrogen underpotential deposition (H_{UPD}) region to the presence of dissolved Fe species (**Figure 7a**). The integrated charge from $0.05 < E_{cathode} < 0.2$ V ($Q_{cathode}$) was stable after the third potential sweep and was inversely proportional to [Fe] but relatively stable with continued cycling. The value of $Q_{cathode}$ for the 0 ppm, 6 ppm, and 24 ppm electrolytes was 8.6, 5.2, and 1.9 mC cm^{-2}, respectively, indicating that the capacitance for H_{UPD} is diminished with increasing [Fe] in the electrolyte and η_{50} shifted negatively by 1.3 mV for every 1 ppm increase in [Fe] **(Figure 7c)**. The voltametric response remained stable over 100 cycles, indicating that continued exposure to Fe-containing electrolytes and potential cycling did not lead to further consumption of active sites for H adsorption. In contrast, cycling from $0.050 < E_{cathode} < 0.500$ V led to an irreversible loss in $Q_{cathode}$ **(Figure S14)**. Thus, although $Q_{cathode}$ decreased by >75% from [Fe] = 0 ppm to 24 ppm, the loss in active surface area did not appear to be caused by continued accumulation of Fe species, consistent with the long-term stability of electrodes operating at $\eta_{cathode} > -120$ mV.
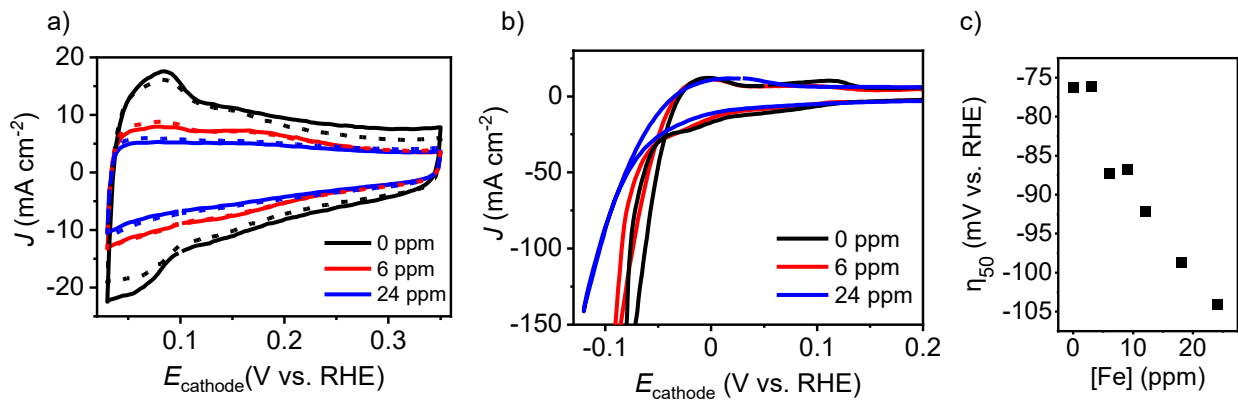

Figure 7: (a) Cyclic voltammetry for a PGM cathode collected at 100 mV s^{-1} in 30% w/w KOH at 80 °C as a function of [Fe]. Dashed lines represent the third cycle and solid lines represent the 100th cycle. **(b)** Cyclic voltammetry of the PGM cathode Fe at 20 mV s^{-1} in 30% w/w KOH at 80

°C with uncoated Ni as the counter electrode. **(c)** *IR*-corrected cathodic overpotential at $J = -50$ mA cm^{-2} in different Fe concentrations.

The specific activity of anodes and cathodes were compared for different electrodes and electrolytes by normalizing the current at a fixed electrode potential by the integrated charge measured in a nearby potential window prior to the onset of electrocatalytic hydrogen or oxygen evolution during linear-sweep voltammetry (**Equations 2, 3**). The anodic sweep was used to measure the charge of the cathode to avoid the influence of the onset of HER.

$$Q_{cathode} = \frac{1}{v} \int_{0.05}^{0.28} J \, dE \qquad (2)$$

$$J_{ECSA} = \frac{J}{Q_c} \qquad (3)$$

For all the anodes, J_Q increased with increasing [Fe] but for the NiCo anode, this increase was offset by a large decrease in Q_{anode} at the highest [Fe] electrolytes. In general, $J_{Q(a)}$ increased by more than one order of magnitude from [Fe] = 0 ppm to 24 ppm. The most-active anode, uncoated Ni in [Fe] = 24 ppm electrolyte, was described by a Q_{anode} that was comparable to the capacitance of as-deposited NiCo and NiO coatings, but this surface coating was generated during operation at the metal mesh. Although coated Ni meshes (NiCo, NiO) provide an initially greater density of electrochemically active metal-oxide and metal-(oxy)hydroxide sites for OER catalysis, the diminished Q_{anode} in the presence of high [Fe] suggests that not all sites remain accessible to electronic- and ionic-conducting pathways necessary to support continuous electrocatalysis. For the PGM electrode, both $Q_{cathode}$ and $J_{(\eta 70)}$ were diminished in a proportional fashion, such that we did not observe a consistent change to $J_{Q(c)}$ with increasing [Fe].

Table 1: Electrochemical behavior of electrodes in 30% w/w KOH as a function of dissolved [Fe]

	0 ppm Fe			6 ppm Fe			24 ppm Fe		
	$J_{(\eta250)}$ (OER) (mA cm^{-2})	Q_{anode} (mC cm^{-2})	$J_{Q(a)}$	$J_{(\eta250)}$ (OER) (mA cm^{-2})	Q_{anode} (mC cm^{-2})	$J_{Q(a)}$	$J_{(\eta250)}$ (OER) (mA cm^{-2})	Q_{anode} (mC cm^{-2})	$J_{Q(a)}$
NiCo	7.4	22.3	0.3	36.4	11.9	3.1	15.0	3.2	4.7
NiO	1.0	36.4	0.02	22.1	40	0.5	67.2	24.8	2.7
Ni	1.8	9.9	0.2	26.4	17.5	1.5	58.8	19.1	3.1
	$J_{(\eta70)}$ (HER) (mA cm^{-2})	$Q_{cathode}$ (mC cm^{-2})	$J_{Q(c)}$	$J_{(\eta70)}$ (HER) (mA cm^{-2})	$Q_{cathode}$ (mC cm^{-2})	$J_{Q(c)}$	$J_{(\eta70)}$ (HER) (mA cm^{-2})	$Q_{cathode}$ (mC cm^{-2})	$J_{Q(c)}$
PGM	133	8.9	14.9	79.6	5.2	15.3	37.1	1.9	19.5

J at OER overpotential (η) = 250 mV, $J_{(\eta250)}$; Absolute J at HER overpotential (η) = –70 mV, $J_{(\eta70)}$; integrated charge under reduction wave at 1.18–1.25 V vs. RHE, Q_{anode}. integrated charge under H_{des} wave at 0.05–0.28 V vs. RHE, $Q_{cathode}$. Current normalized activity for anodes, $J_{Q(a)}$ and for cathodes, $J_{Q(c)}$ (mA mC^{-1}).

Discussion

Influence of Fe on the polarization response of electrolysis cells

The AAWE cell potential, E_{cell}, includes the thermodynamic potential for water splitting at the operating temperature and pressure, $E^{o'}(T,P)$, the ohmic voltage loss, equal to the operating J times the area-specific cell resistance R_Ω (Ω cm^2), and the overpotentials at the anode and cathode (**Equation 4**).

$$E_{cell}(J) = E^{o'}(T,P) + JR_\Omega + \eta_{anode}(J) - \eta_{cathode}(J) \tag{4}$$

R_Ω is dominated by ionic resistance across the electrolyte and separator and is not expected to vary substantially with [Fe] unless there is an accumulation of Fe-containing precipitates within the microporous separator. A PGM-NiCo cell operated at 80 °C was optimized when the [Fe] = 6

ppm, yielding E_{cell} = 1.77(7) V at J = 250 mA cm^{-2}, which is greater than the [Fe] expected for purified KOH electrolytes but less than the solubility limit of [Fe], indicating that judicious control of dissolved Fe provides a route to optimize cell performance. In general, the effect of Fe on E_{cell} is lesser as cell temperature increases, with 200–250 mV improvements in E_{cell} observed via control of [Fe] at 20 °C as compared to a ~100 mV improvement to E_{cell} at 80 °C. Consistent with previous studies at uncoated Ni electrodes[24,36,37] and studies on thin film $Ni_zFe_{1-z}O_x(OH)_y$ in 1 M $KOH_{(aq)}$[22,38,39] we find that increasing [Fe] leads to a substantial negative shift in η_{anode} at uncoated Ni and NiO electrodes up to the point of Fe precipitation within the electrolyte. Increasing [Fe] also leads to changes to the electrochemically active surface area which can partially or wholly offset improvements in local electrocatalyst activity (**Figure 4**).

Influence of dissolved Fe on anode catalyst coatings

Consistent with previous studies on thick NiO_x films tested in 1 M KOH, the effects of Fe on the ECSA and η_{anode} were found to depend on the initial composition and thickness of the catalyst coating.[31] Previous studies on co-deposited nickel-iron (oxy)hydroxide films showed that thin films with Ni:Fe = 3:1 exhibited the maximum OER activity on a per-metal basis.[22] We find that $NiCoO_xH_y$-coated anodes yielded the lowest η_{anode} at low [Fe]—where the deleterious impact of Fe on the cathode is marginal (< 10 mV)—whereas the lowest overall η_{anode} was obtained at a NiO-coated Ni mesh tested in a Fe-rich electrolyte (**Figure 4**, **Table S3**). These results are consistent with extensive research showing that NiO_xH_y is a poor OER catalyst in the absence of Fe but that Ni(Fe)OOH is the most effective OER catalyst in alkaline environments.[22,39] The lesser effect of [Fe] on η_{anode} at elevated temperatures is likely related to the expected exponential increase in reaction kinetics with increasing temperature as well as a reduced tendency for more-soluble Fe to partition to the catalyst surface.[6,7,40] Surprisingly, Ni electrodes exhibited comparable

electrochemically active surface areas during extended testing in Fe-rich, concentrated KOH despite the initially greater Q_{anode} for NiO anodes.

The effect of [Fe] on transition-metal-oxide anode catalysts is evident in changes in the anodic peak potential, E_p^a, and integrated charge, Q_{anode}, of redox peaks before the OER. As the [Fe] was increased, Q_{anode} decreased for anodes coated with NiO and NiCo but increased for Ni. Previous studies on thin film NiCo oxide reported anodic shifts in E_p^a in the presence of dissolved Fe.[22,30]. A positive shift in E_p^c in the presence of increasing [Fe] is qualitatively consistent with an increase in the Fe composition within the catalyst.[41] In contrast, thick NiCo coatings yielded a single, broad anodic peak from E = 1.23–1.35 V which initially did not shift substantially with increasing [Fe] (**Figure 4**). Moreover, at high [Fe], Q_{anode} decreases by over 80% relative to Fe-free electrolytes indicating a loss of electroactive material within the anode coating. The intensity of Raman peaks associated with Ni-O vibrations within oxyhydroxide phases decreased when [Fe] was increased from 6 ppm to 24 ppm which is consistent with the decrease in Q_{anode}. At low Fe concentrations [Fe] < 24 ppm, both NiO and Ni electrodes showed changes in both E_p^a and Q_{anode} consistent with structural transformations from NiO_xH_y to NiOOH that directly correlate to the increase in Q_{anode} and increased OER activity. At [Fe] = 24 ppm, the Q_{anode} of NiO electrode shows a decrease (~ 30%) whereas the Ni electrode showed an increasing Q_{anode} with increasing [Fe] to the soluble limit.

The changes to the electrochemical behavior of Ni-based anodes in the presence of dissolved Fe may be understood through at least three possible mechanisms: (i) Fe can induce structural changes leading to loss of catalyst material from the electrode surface (ii) supersaturated [Fe] can precipitate to form ionically insulating phases that block active redox-active sites (iii) Fe incorporation shifts the potential needed to oxidize metal hydroxides into the electrically

conducting 3+ state to more positive potentials. Visual evidence of catalyst delamination and changes to Q_{anode} were not apparent within 2 voltammetry cycles, and so we focus our discussion on mechanisms (ii-iii).

Changes in the electrical response of the catalyst layer could be induced by Fe incorporation within the film. NiO_xH_y films are substantially more electrically conductive when oxidized from the 2+ to 3+ oxidation state, as in $Ni(OH)_2$ or NiO, which enables reactivity across the electrocatalytic activity of the molecularly porous surface active oxyhydroxide layer that grows on metal or metal oxide electrodes under alkaline water oxidation conditions. However, upon reduction, Ni^{3+} transforms back to $Ni(OH)_2$ phases which are comparatively more electrically insulating.[42] The potential required to re-oxidize Ni-based catalyst layers into a conducting state shifts positively with increasing Fe content within the film.[22] The presence of Raman peaks corresponding to Ni-O vibrations at a potential before the $Ni^{2+/3+}$ oxidation peak for [Fe] = 6, 24 ppm suggests the formation of electrochemically trapped Ni^{3+} species on the catalyst surface. Likewise, thin films of cobalt oxides cycled in the presence of dissolved Fe show a positive shift in the redox wave associated with $Co^{2+/3+}$ transitions and the through-film conductivity at $E_{anode} =$ 0.4 V vs Hg/HgO in 1 M $KOH_{(aq)}$ is reduced by $\sim10^3$ for CoO_x films containing 54% Fe.[43] We hypothesize that electrodeposited NiO and NiCo catalyst layers undergoing potential cycling in the presence of high [Fe] may form Fe-rich phases which prevent oxidation in the potential range required to catalyze the OER in more active regions of the film. This is consistent with the observed reduction in Q_{anode} and reduced Raman intensity for Ni-O vibrations in NiOOH for coated anodes in the presence of high [Fe] despite the monotonic increase in J_Q for all anodes with increasing [Fe] (**Figure 5c, Table S4**).

Ex-situ Raman measurements of the NiCo surface after testing in high [Fe] electrolytes indicate the possible formation of α-Fe_2O_3 on the surface, which could mask the active catalyst

layer lower the apparent ECSA.[44–46] α-Fe$_2$O$_3$ was observed in the NiCo sample tested in [Fe] = 24 ppm but not for an electrode tested in [Fe] = 6 ppm (**Figure S15**). However, Raman peaks associated with either α-Fe$_2$O$_3$ or FeOOH were not detected for electrodes monitored in an operational cell environment across a wide range of E and [Fe] (**Figure 5c**, **Figure S13**), suggesting that α-Fe$_2$O$_3$ is formed *ex-situ*. These data are more consistent where passivation occurs with the formation of Fe-rich NiOOH phases but other bulk Fe (oxy)(hydr)oxide phases with weak Raman scattering intensities, such as Fe(OH)$_2$ may have been present on the electrode surface. We observe changes in the relative intensities of the Ni-O peaks associated bending and stretching modes as a function of [Fe] (**Table S4**). These changes have previously been attributed to transitions between γ-NiOOH and β-NiOOH phases, but since these peak intensities are sensitive to multiple factors we do not make claims about the specific phase of the Fe-doped NiCoO$_x$H$_y$ films tested at increased [KOH] and T relative to previous works.[33,47]

Influence of dissolved Fe on cathode catalyst coatings

The effect of Fe on AWE cathodes depends sensitively on the operating potential of the HER catalyst. Increasing [Fe] led to consistent loss in Pt active sites for hydrogen evolution, as measured by $Q_{cathode}$ in the H$_{UPD}$ region (**Figure 6**) and this change was commensurate with a more negative $\eta_{cathode}$. These results stand in contrast with those observed for lower-activity Ni cathodes where previous studies at uncoated Ni cathodes with $\eta_{cathode}$ more negative than –335 mV at J = 250 mA cm^{-2} found that [Fe] = 14 ppm led to improved overpotentials for the HER. This difference is likely related to the fact that highly active cathodes for AWE operate at $\eta_{cathode}$ more positive than –120 mV vs. RHE, a potential positive of that required for the electrodeposition of metallic Fe. Although increasing [Fe] leads to an increasingly negative shift in $\eta_{cathode}$ for all [Fe], this shift stabilized within 30 min of Fe spiking and does not worsen over continued cathodic bias the ~50 h of the tests here, suggesting that no further effect on HER was observed for electrode potentials

22

positive of Fe metal deposition. Thus, whereas less-active transition-metal cathodes may facilitate electrodeposition of Fe and Fe-oxide species that can activate the alkaline HER (leading to a lower E_{cell}), platinum-group-metal operate at potentials positive of that required to electrodeposit Fe and are primarily impacted by dissolved or weakly adsorbed Fe species which lead to a modest (≤ 30 mV) increase in E_{cell} that is proportional to [Fe].[26,48]

Implications for the design of advanced alkaline water electrolysis cells

Together, these findings suggest that the composition of catalyst coatings can be modulated for peak performance at varied [Fe], with low [Fe] being potentially desirable for high-activity cathodes, and that anode designs for Fe-rich electrolytes may reach lower overpotentials through judicious control of the metal-mesh precursor and supporting cations rather than through control of coating composition and thickness.

In this work, we have only studied the effect of Fe on the electrodes in a stagnant electrolyte. However, persistent, high levels of [Fe] may lead to precipitation that reduces the porosity of the separator and hence affects increases R_Ω and E_{cell}. Industrial AWE cells are operated for 1000s of hours with a recirculated electrolyte which may accumulate dissolved Fe via corrosion of pipes, gas-liquid separators, and other components external to the stack. In addition, a circulating dissolved Fe feed could lead to continuous accumulation at both the anode and cathode leading to durability issues that are not tested and are outside the scope of this manuscript. Future studies should consider circulating KOH systems and the effects of total Fe on all cell components including porous separators and ion exchange membranes.

Conclusion

In summary, the presence of dissolved Fe in AAWE cells consistently improved the overall efficiency for water electrolysis relative to Fe-free cells. This is due to the more substantial benefits

of dissolved Fe at Ni-based anode catalysts compared to modest deleterious effects at PGM-containing cathode coatings. The magnitude of this improvement is controlled by the cell operating temperature, with the shifts in E_{cell} as large as 250 mV (>10% of the operating voltage) for cells operated at 20 °C. AWE cells operated at industrially relevant temperatures (80 °C) afford lower values of E_{cell} but these are still improved by as much as 100 mV through judicious control of [Fe] (**Figure 2a**). The total improvement to E_{cell} is determined by a balance between Fe incorporation into transition metal oxides to form OER-active oxyhydroxide species, and the loss of HER-active surface sites at PGM-containing cathode coatings. Co-design of anode meshes, OER electrocatalysts formed during operation at low [Fe], and cathodes that are tolerant to increased [Fe] within the electrolyte are expected to lead to further reductions in the total activation overpotential for advanced alkaline water electrolyzer cells. Together, this work shows that controlling Fe impurities in advanced alkaline water electrolyzers is a key tool in designing higher performance systems.

Supporting information

Additional experimental details, supporting data, and additional figures including electron-microscopy and elemental analysis, x-ray photoelectron spectra, diffraction patterns, Tafel plots, and Raman spectra.

Acknowledgments

and the Center for Advanced Materials Characterization in Oregon (CAMCOR) for assistance with XPS measurement and analysis. We thank Dr. Grace Lindquist for helpful discussions on liquid alkaline electrolyzer electrodes and systems operation and Julian McAdams for assistance with zero-gap cell manufacture.

Notes

References

(1) Chatenet, M.; G. Pollet, B.; R. Dekel, D.; Dionigi, F.; Deseure, J.; Millet, P.; D. Braatz, R.; Z. Bazant, M.; Eikerling, M.; Staffell, I.; Balcombe, P.; Shao-Horn, Y.; Schäfer, H. Water Electrolysis: From Textbook Knowledge to the Latest Scientific Strategies and Industrial Developments. *Chem. Soc. Rev.* **2022**, *51* (11), 4583–4762. https://doi.org/10.1039/D0CS01079K.
(2) Tilak, B. V.; Lu, P. W. T.; Colman, J. E.; Srinivasan, S. Electrolytic Production of Hydrogen. In *Comprehensive Treatise of Electrochemistry: Electrochemical Processing*; Bockris, J. O.,

Conway, B. E., Yeager, E., White, R. E., Eds.; Comprehensive Treatise of Electrochemistry; Springer US: Boston, MA, 1981; pp 1–104. https://doi.org/10.1007/978-1-4684-3785-0_1.

(3) IRENA. *Green Hydrogen Cost Reduction*; IRENA, 2020. https://www.irena.org/Publications/2020/Dec/Green-hydrogen-cost-reduction (accessed 2023-05-24).

(4) Pletcher, D.; Li, X.; Wang, S. A Comparison of Cathodes for Zero Gap Alkaline Water Electrolysers for Hydrogen Production. *Int. J. Hydrog. Energy* **2012**, *37* (9), 7429–7435. https://doi.org/10.1016/j.ijhydene.2012.02.013

(5) Trotochaud, L.; Ranney, J. K.; Williams, K. N.; Boettcher, S. W. Solution-Cast Metal Oxide Thin Film Electrocatalysts for Oxygen Evolution. *J. Am. Chem. Soc.* **2012**, *134* (41), 17253–17261. https://doi.org/10.1021/ja307507a.

(6) Hall, D. E. Alkaline Water Electrolysis Anode Materials. *J. Electrochem. Soc.* **1985**, *132* (2), 41C.

(7) Wendt, H.; Imarisio, G. Nine Years of Research and Development on Advanced Water Electrolysis. A Review of the Research Programme of the Commission of the European Communities. *J. Appl. Electrochem.* **1988**, *18* (1), 1–14. https://doi.org/10.1007/BF01016198.

(8) Karacan, C.; Lohmann-Richters, F. P.; Shviro, M.; Keeley, G. P.; Müller, M.; Carmo, M.; Stolten, D. Fabrication of High Performing and Durable Nickel-Based Catalyst Coated Diaphragms for Alkaline Water Electrolyzers. *J. Electrochem. Soc.* **2022**, *169* (5), 054502. https://doi.org/10.1149/1945-7111/ac697f.

(9) Mergel, J.; Carmo, M.; Fritz, D. Status on Technologies for Hydrogen Production by Water Electrolysis. In *Transition to Renewable Energy Systems*; Stolten, D., Scherer, V., Eds.; Wiley, 2013; pp 423–450. https://doi.org/10.1002/9783527673872.ch22.

(10) Phillips, R.; Dunnill, C. W. Zero Gap Alkaline Electrolysis Cell Design for Renewable Energy Storage as Hydrogen Gas. *RSC Adv.* **2016**, *6* (102), 100643–100651. https://doi.org/10.1039/C6RA22242K.

(11) Kraglund, M. R.; Carmo, M.; Schiller, G.; Ansar, S. A.; Aili, D.; Christensen, E.; Jensen, J. O. Ion-Solvating Membranes as a New Approach towards High Rate Alkaline Electrolyzers. *Energy Environ. Sci.* **2019**, *12* (11), 3313–3318. https://doi.org/10.1039/C9EE00832B.

(12) de Groot, M. T.; Kraakman, J.; Garcia Barros, R. L. Optimal Operating Parameters for Advanced Alkaline Water Electrolysis. *Int. J. Hydrog. Energy* **2022**, *47* (82), 34773–34783. https://doi.org/10.1016/j.ijhydene.2022.08.075.

(13) Goyal, A.; Louisia, S.; Moerland, P.; Koper, M. T. M. Cooperative Effect of Cations and Catalyst Structure in Tuning Alkaline Hydrogen Evolution on Pt Electrodes. *J. Am. Chem. Soc.* **2024**, *146* (11), 7305–7312. https://doi.org/10.1021/jacs.3c11866.

(14) Ringe, S. Cation Effects on Electrocatalytic Reduction Processes at the Example of the Hydrogen Evolution Reaction. *Curr. Opin. Electrochem.* **2023**, *39*, 101268. https://doi.org/10.1016/j.coelec.2023.101268.

(15) Bender, J. T.; Petersen, A. S.; Østergaard, F. C.; Wood, M. A.; Heffernan, S. M. J.; Milliron, D. J.; Rossmeisl, J.; Resasco, J. Understanding Cation Effects on the Hydrogen Evolution Reaction. *ACS Energy Lett.* **2023**, *8* (1), 657–665. https://doi.org/10.1021/acsenergylett.2c02500.

(16) Monteiro, M. C. O.; Goyal, A.; Moerland, P.; Koper, M. T. M. Understanding Cation Trends for Hydrogen Evolution on Platinum and Gold Electrodes in Alkaline Media. *ACS Catal.* **2021**, *11* (23), 14328–14335. https://doi.org/10.1021/acscatal.1c04268.

(17) Mahmood, N.; Yao, Y.; Zhang, J.; Pan, L.; Zhang, X.; Zou, J. Electrocatalysts for Hydrogen Evolution in Alkaline Electrolytes: Mechanisms, Challenges, and Prospective Solutions. *Adv. Sci.* **2018**, *5* (2), 1700464. https://doi.org/10.1002/advs.201700464.

(18) Xue, S.; Garlyyev, B.; Watzele, S.; Liang, Y.; Fichtner, J.; Pohl, M. D.; Bandarenka, A. S. Influence of Alkali Metal Cations on the Hydrogen Evolution Reaction Activity of Pt, Ir, Au, and Ag Electrodes in Alkaline Electrolytes. *ChemElectroChem* **2018**, *5* (17), 2326–2329. https://doi.org/10.1002/celc.201800690.

(19) Zaffran, J.; Stevens, M. B.; Trang, C. D. M.; Nagli, M.; Shehadeh, M.; Boettcher, S. W.; Caspary Toroker, M. Influence of Electrolyte Cations on Ni(Fe)OOH Catalyzed Oxygen Evolution Reaction. *Chem. Mater.* **2017**, *29* (11), 4761–4767. https://doi.org/10.1021/acs.chemmater.7b00517.

(20) Garcia, A. C.; Touzalin, T.; Nieuwland, C.; Perini, N.; Koper, M. T. M. Enhancement of Oxygen Evolution Activity of Nickel Oxyhydroxide by Electrolyte Alkali Cations. *Angew. Chem. Int. Ed.* **2019**, *58* (37), 12999–13003. https://doi.org/10.1002/anie.201905501.

(21) Corrigan, D. A. The Catalysis of the Oxygen Evolution Reaction by Iron Impurities in Thin Film Nickel Oxide Electrodes. *J. Electrochem. Soc.* **1987**, *134* (2), 377. https://doi.org/10.1149/1.2100463.

(22) Trotochaud, L.; Young, S. L.; Ranney, J. K.; Boettcher, S. W. Nickel–Iron Oxyhydroxide Oxygen-Evolution Electrocatalysts: The Role of Intentional and Incidental Iron Incorporation. *J. Am. Chem. Soc.* **2014**, *136* (18), 6744–6753. https://doi.org/10.1021/ja502379c.

(23) Ou, Y.; Twight, L. P.; Samanta, B.; Liu, L.; Biswas, S.; Fehrs, J. L.; Sagui, N. A.; Villalobos, J.; Morales-Santelices, J.; Antipin, D.; Risch, M.; Toroker, M. C.; Boettcher, S. W. Cooperative Fe Sites on Transition Metal (Oxy)Hydroxides Drive High Oxygen Evolution Activity in Base. *Nat. Commun.* **2023**, *14* (1), 7688. https://doi.org/10.1038/s41467-023-43305-z.

(24) Demnitz, M.; Lamas, Y. M.; Garcia Barros, R. L.; De Leeuw Den Bouter, A.; Van Der Schaaf, J.; Theodorus De Groot, M. Effect of Iron Addition to the Electrolyte on Alkaline Water Electrolysis Performance. *iScience* **2024**, *27* (1), 108695. https://doi.org/10.1016/j.isci.2023.108695.

(25) Xue, S.; Haid, R. W.; Kluge, R. M.; Ding, X.; Garlyyev, B.; Fichtner, J.; Watzele, S.; Hou, S.; Bandarenka, A. S. Enhancing the Hydrogen Evolution Reaction Activity of Platinum Electrodes in Alkaline Media Using Nickel–Iron Clusters. *Angew. Chem. Int. Ed.* **2020**, *59* (27), 10934–10938. https://doi.org/10.1002/anie.202000383.

(26) Nidola, A.; Schira, R. Poisoning Mechanisms and Structural Analyses on Metallic Contaminated Cathode Catalysts in Chlor-Alkali Membrane Cell Technology. *J. Electrochem. Soc.* **1986**, *133* (8), 1653. https://doi.org/10.1149/1.2108984.

(27) *NRG® (Hydrogen Generation Products) | De Nora*. denora. https://www.denora.com/our-brands/NRG.html (accessed 2024-06-07).

(28) Oda, K.; Kuroda, Y.; Mitsushima, S. Investigation of Charge–Discharging Behavior of Metal Oxide–Based Anode Electrocatalysts for Alkaline Water Electrolysis to Suppress Degradation Due to Reverse Current. *Electrocatalysis* **2023**, *14* (3), 499–510. https://doi.org/10.1007/s12678-023-00815-0.

(29) Abdel Haleem, A.; Huyan, J.; Nagasawa, K.; Kuroda, Y.; Nishiki, Y.; Kato, A.; Nakai, T.; Araki, T.; Mitsushima, S. Effects of Operation and Shutdown Parameters and Electrode Materials on the Reverse Current Phenomenon in Alkaline Water Analyzers. *J. Power Sources* **2022**, *535*, 231454. https://doi.org/10.1016/j.jpowsour.2022.231454.

(30) Burke, M. S.; Kast, M. G.; Trotochaud, L.; Smith, A. M.; Boettcher, S. W. Cobalt–Iron (Oxy)Hydroxide Oxygen Evolution Electrocatalysts: The Role of Structure and Composition on Activity, Stability, and Mechanism. *J. Am. Chem. Soc.* **2015**, *137* (10), 3638–3648. https://doi.org/10.1021/jacs.5b00281.

(31) Batchellor, A. S.; Boettcher, S. W. Pulse-Electrodeposited Ni–Fe (Oxy)Hydroxide Oxygen Evolution Electrocatalysts with High Geometric and Intrinsic Activities at Large Mass Loadings. *ACS Catal.* **2015**, *5* (11), 6680–6689. https://doi.org/10.1021/acscatal.5b01551.

(32) Dionigi, F.; Zhu, J.; Zeng, Z.; Merzdorf, T.; Sarodnik, H.; Gliech, M.; Pan, L.; Li, W.-X.; Greeley, J.; Strasser, P. Intrinsic Electrocatalytic Activity for Oxygen Evolution of Crystalline 3d-Transition Metal Layered Double Hydroxides. *Angew. Chem. Int. Ed Engl.* **2021**, *60* (26), 14446–14457. https://doi.org/10.1002/anie.202100631.

(33) Klaus, S.; Cai, Y.; Louie, M. W.; Trotochaud, L.; Bell, A. T. Effects of Fe Electrolyte Impurities on Ni(OH)2/NiOOH Structure and Oxygen Evolution Activity. *J. Phys. Chem. C* **2015**, *119* (13), 7243–7254. https://doi.org/10.1021/acs.jpcc.5b00105.

(34) Gallenberger, J.; Fernández, H. M.; Alkemper, A.; Li, M.; Tian, C.; Kaiser, B.; Philipp Hofmann, J. Stability and Decomposition Pathways of the NiOOH OER Active Phase of NiO x Electrocatalysts at Open Circuit Potential Traced by Ex Situ and in Situ Spectroscopies. *Catal. Sci. Technol.* **2023**, *13* (16), 4693–4700. https://doi.org/10.1039/D3CY00674C.

(35) Allanore, A.; Lavelaine, H.; Valentin, G.; Birat, J. P.; Lapicque, F. Electrodeposition of Metal Iron from Dissolved Species in Alkaline Media. *J. Electrochem. Soc.* **2007**, *154* (12), E187. https://doi.org/10.1149/1.2790285.

(36) Huot, J.-Y. Hydrogen Evolution and Interface Phenomena on a Nickel Cathode in 30 w/o KOH : I . Kinetics Parameters and Electrode Impedance Between 303 and 363 K. *J. Electrochem. Soc.* **1989**, *136* (7), 1933. https://doi.org/10.1149/1.2097088.

(37) Brossard, L.; Huot, J.-Y. In Situ Activation of Cathodes during Alkaline Water Electrolysis by Dissolved Iron and Molybdenum Species. *J. Appl. Electrochem.* **1991**, *21* (6), 508–515. https://doi.org/10.1007/BF01018603.

(38) Twight, L.; Tonsberg, A.; Samira, S.; Velinkar, K.; Dumpert, K.; Ou, Y.; Wang, L.; Nikolla, E.; Boettcher, S. Trace Fe in Alkaline Electrolyte Governs the OER Activity of Perovskite LaNiO3 and La2NiO4 via Interaction with Redox-Active Surface NiOxHy Formed by Applied Bias. October 4, 2023. https://doi.org/10.26434/chemrxiv-2023-0rd31.

(39) Krivina, R. A.; Ou, Y.; Xu, Q.; Twight, L. P.; Stovall, T. N.; Boettcher, S. W. Oxygen Electrocatalysis on Mixed-Metal Oxides/Oxyhydroxides: From Fundamentals to Membrane Electrolyzer Technology. *Acc. Mater. Res.* **2021**, *2* (7), 548–558. https://doi.org/10.1021/accountsmr.1c00087.

(40) Beverskog, B.; Puigdomenech, I. Revised Pourbaix Diagrams for Iron at 25–300 C. *Corros. Sci.* **1996**, *38* (12), 2121–2135.

(41) Magnier, L.; Cossard, G.; Martin, V.; Pascal, C.; Roche, V.; Sibert, E.; Shchedrina, I.; Bousquet, R.; Parry, V.; Chatenet, M. Fe–Ni-Based Alloys as Highly Active and Low-Cost Oxygen Evolution Reaction Catalyst in Alkaline Media. *Nat. Mater.* **2024**, *23* (2), 252–261. https://doi.org/10.1038/s41563-023-01744-5.

(42) Batchellor, A.; Kwon, G.; Laskowski, F.; Tiede, D.; Boettcher, S. Domain Structures of Ni and NiFe (Oxy)Hydroxide Oxygen-Evolution Catalysts from X-Ray Pair Distribution Function Analysis. *J. Phys. Chem. C* **2017**, *121*. https://doi.org/10.1021/acs.jpcc.7b10306.

(43) Burke, M. S.; Kast, M. G.; Trotochaud, L.; Smith, A. M.; Boettcher, S. W. Cobalt–Iron (Oxy)Hydroxide Oxygen Evolution Electrocatalysts: The Role of Structure and

Composition on Activity, Stability, and Mechanism. *J. Am. Chem. Soc.* **2015**, *137* (10), 3638–3648. https://doi.org/10.1021/jacs.5b00281.

(44) Chen, Z.; Cai, L.; Yang, X.; Kronawitter, C.; Guo, L.; Shen, S.; Koel, B. E. Reversible Structural Evolution of NiCoO $_x$ H $_y$ during the Oxygen Evolution Reaction and Identification of the Catalytically Active Phase. *ACS Catal.* **2018**, *8* (2), 1238–1247. https://doi.org/10.1021/acscatal.7b03191.

(45) Liu, Y.; Smith, R. D. L. Identifying Protons Trapped in Hematite Photoanodes through Structure–Property Analysis. *Chem. Sci.* **2020**, *11* (4), 1085–1096. https://doi.org/10.1039/C9SC04853G.

(46) de Faria, D. L. A.; Venâncio Silva, S.; de Oliveira, M. T. Raman microspectroscopy of some iron oxides and oxyhydroxides. *J. Raman Spectrosc.* **1997**, *28* (11), 873–878. https://doi.org/10.1002/(SICI)1097-4555(199711)28:11<873::AID-JRS177>3.0.CO;2-B.

(47) Kostecki, R.; McLarnon, F. Electrochemical and In Situ Raman Spectroscopic Characterization of Nickel Hydroxide Electrodes: I. Pure Nickel Hydroxide. *J. Electrochem. Soc.* **1997**, *144* (2), 485. https://doi.org/10.1149/1.1837437.

(48) Subbaraman, R.; Tripkovic, D.; Chang, K.-C.; Strmcnik, D.; Paulikas, A. P.; Hirunsit, P.; Chan, M.; Greeley, J.; Stamenkovic, V.; Markovic, N. M. Trends in Activity for the Water Electrolyser Reactions on 3d M(Ni,Co,Fe,Mn) Hydr(Oxy)Oxide Catalysts. *Nat. Mater.* **2012**, *11* (6), 550–557. https://doi.org/10.1038/nmat3313.

Table of Contents